Nuclear Instruments and Methods in Physics Research A 765 (2014) 275–279

Contents lists available at ScienceDirect

Nuclear Instruments and Methods in Physics Research A

journal homepage: www.elsevier.com/locate/nima

Qualification test of a MPPC-based PET module for future MRI-PET scanners

Y. Kurei [a,*], J. Kataoka [a], T. Kato [a], T. Fujita [a], H. Funamoto [a], T. Tsujikawa [a], S. Yamamoto [b]

[a] Research Institute for Science and Engineering, Waseda University, 3-4-1, Ohkubo, Shinjuku, Tokyo, Japan
[b] Department of Radiological and Medical Laboratory Sciences, Nagoya University Graduate School of Medicine, 65-banchi, Tsurumai-cho, Showa-ku, Nagoya-shi, Aichi, Japan

ARTICLE INFO

Available online 28 April 2014

Keywords:
Multi-Pixel Photon Counter (MPPC)
Positron Emission Tomography (PET)
Magnetic Resonance Imaging (MRI)

ABSTRACT

We have developed a high-resolution, compact Positron Emission Tomography (PET) module for future use in MRI-PET scanners. The module consists of large-area, 4 × 4 ch MPPC arrays (Hamamatsu S11827-3344MG) optically coupled with Ce:LYSO scintillators fabricated into 12 × 12 matrices of 1 × 1 mm^2 pixels. At this stage, a pair of module and coincidence circuits was assembled into an experimental prototype gantry arranged in a ring of 90 mm in diameter to form the MPPC-based PET system. The PET detector ring was then positioned around the RF coil of the 4.7 T MRI system. We took an image of a point ^{22}Na source under fast spin echo (FSE) and gradient echo (GE), in order to measure interference between the MPPC-based PET and the MRI. We only found a slight degradation in the spatial resolution of the PET image from 1.63 to 1.70 mm (FWHM; *x*-direction), or 1.48–1.55 mm (FWHM; *y*-direction) when operating with the MRI, while the signal-to-noise ratio (SNR) of the MRI image was only degraded by 5%. These results encouraged us to develop a more advanced version of the MRI-PET gantry with eight MPPC-based PET modules, whose detailed design and first qualification test are also presented in this paper.

1. Introduction

Positron Emission Tomography (PET) imaging is a method of detecting cancers and diagnosing Alzheimer's disease in its early stages [1]. In particular, the idea of combining PET giving physiological information with the imaging devices giving anatomical information is very effective because we can identify anatomical locations and fix the position of cancer more precisely. This idea has already been put to practical use as PET-CT, but PET-CT has a problem regarding double exposure, that is, internal exposure by PET and external exposure by X-ray CT. In order to solve this problem, there has been much excitement about the recent development of MRI-PET: MRI is used in place of X-ray CT [2–6]. However, a Photo-Multiplier Tube (PMT) often used in PET scanners is difficult to operate within high magnetic fields. Using a semiconductor detector instead PMT can overcome this problem. We have developed APD-based PET scanners, and a spatial resolution of 0.9 mm (FWHM) was obtained from filter back projection (FBP) reconstructed images in preliminary experiments with a centrally positioned ^{22}Na point source (0.25 mm ϕ) [7].

The Multi-Pixel Photon Counter (MPPC) is a compact type of high performance semiconductor photo-detector consisting of multiple Geiger-mode APD pixels and a promising photo-detector for PET. MPPC has high gain comparable to that of PMT, which results in a good signal-to-noise (S/N) ratio. Also, it does not need a charge-sensitive amplifier, which results in better timing resolution [8]. In addition, MPPCs are very compact sensors and insensitive to magnetic fields in theory. These great advantages can be applied not only to MRI-PET but also to Time-of-Flight (ToF) or Depth-of-Interaction (DoI) applications. For example, we have developed a front-end ASIC for future PET scanners [9] that offers ToF capability in conjunction with a MPPC array, and obtained time jitter and walk measurement of 67 ps and 98 ps (FWHM), respectively. The coincidence timing resolution between two MPPCs coupled with LYSO scintillators was then revealed as 491 ps (FWHM). Moreover, we proposed a novel technique of measuring the 3-D positions of gamma-ray absorption based on MPPC arrays and scintillator blocks [10]. This technique can be widely used for vast applications including DoI-PET [11]. In following such research, we have been developing MRI-PET—a next-generation PET system. This paper describes our measurements of simultaneous PET and MR imaging, and evaluates the interference between PET and MRI systems.

2. Experimental setup

2.1. PET images operating with MRI

Fig. 1 (left) shows the MPPC-based PET module that we developed. This module consists of large-area, 4 × 4 ch MPPC arrays (Fig. 1

* Corresponding author.
E-mail address: yk-3562.mss@toki.waseda.jp (Y. Kurei).

http://dx.doi.org/10.1016/j.nima.2014.04.040
0168-9002/

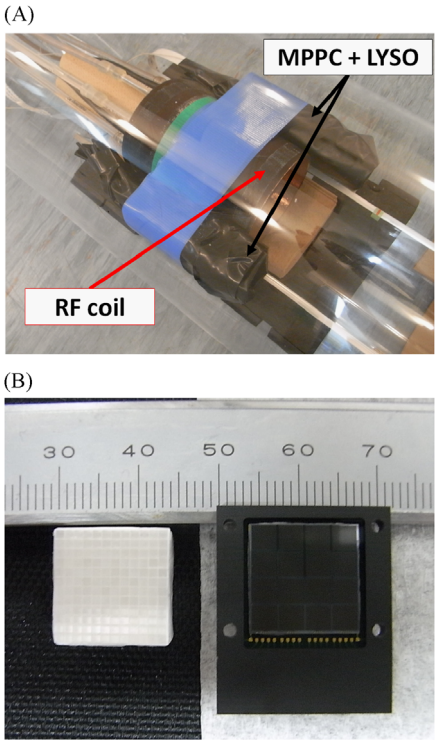

Fig. 1. Left: A pair of MPPC modules was positioned around the RF coil. Right: LYSO scintillator array and MPPC array. This scintillator array is fabricated into 12×12 matrices of 1×1 mm pixels. The MPPC array is the model number of S11827-3344MG (Hamamatsu Photonics K.K.).

Table 1
Basic characteristics of MPPC at + 25 °C.

Parameters	Specification
Number of elements (ch)	4×4
Effective active area/channel (mm)	3×3
Pixel size of a Geiger-mode APD (μm)	50
Number of pixels/channel	3600
Typical photon detection efficiency (λ=440 nm) (%)	50
Typical dark count rates/channel (kcps)	$\lesssim 400$
Terminal capacitance/channel (pF)	320
Gain (at operation voltage)	7.5×10^5

Table 2
Basic characteristics of Ce:LYSO scintillator.

	Ce:LYSO
Density (g/cm^3)	7.10
Light yield (photons/MeV)	25,000
Decay time (ns)	40
Peak wavelength (nm)	420

(right); S11827-3344MG, Hamamatsu Photonics K.K., Japan) optically coupled with a Ce-doped $(Lu, Y)_2(SiO_4)O$ (Ce:LYSO) scintillator array with an acrylic light guide 1-mm thick, which distributes scintillator photons across multiple MPPC array channels. Tables 1 and 2 list the basic characteristics of the MPPC array [12–14] and Ce:LYSO [15], respectively. These scintillators are fabricated into 12×12 matrices of $1 \times 1 \times 10$ mm^3 pixels (Fig. 1 left). Each scintillator pixel is divided and coated with a reflective $BaSO_4$ layer of 0.2-mm thick. A pair of modules was also assembled into an experimental prototype gantry arranged in a ring of 90 mm in diameter to form the MPPC-based PET system. The PET detector ring was then positioned around a radio-frequency (RF) coil of the 4.7 T MRI system.

Fig. 2 shows the experimental setup used for the imaging tests of PET and the block diagram of this experiment. The 16 signals from one MPPC module passed through flexible flat cables and were processed by a resistive charge division network [16–18] outside the MRI. Fig. 3 shows the resistor network circuit that we used, as discussed in detail in Ref. [19]. This resistor network was applied by using a charge division readout technique, which we used to compile 16 signals into four position-encoded signals. The four signals from one resistor network were fed into Quad Linear FAN IN/OUT (Phillips MODEL 6954) and divided into two lines. One

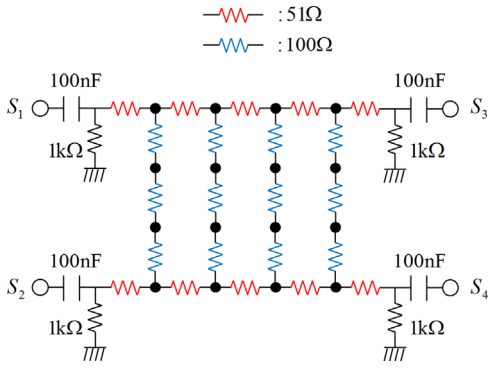

Fig. 3. The charge division resistor network. Sixteen anodes of the MPPC array are directly connected to the black circles.

Table 3
Parameters used for FSEMS and GEMS.

	FSEMS	GEMS
Pulse form	Gaussian	Sinc
Pulse width	1000 μs	2000 μs
Repetition time	2000 ms	100 ms
Echo time	12 ms	10 ms
Flip angle	–	45 deg.
Slice FoV	5.0×5.0 cm^2	5.0×5.0 cm^2
Slice matrix	256×128	256×128
Scan	10.5 min. (NEX 20)	10.3 min. (NEX 48)

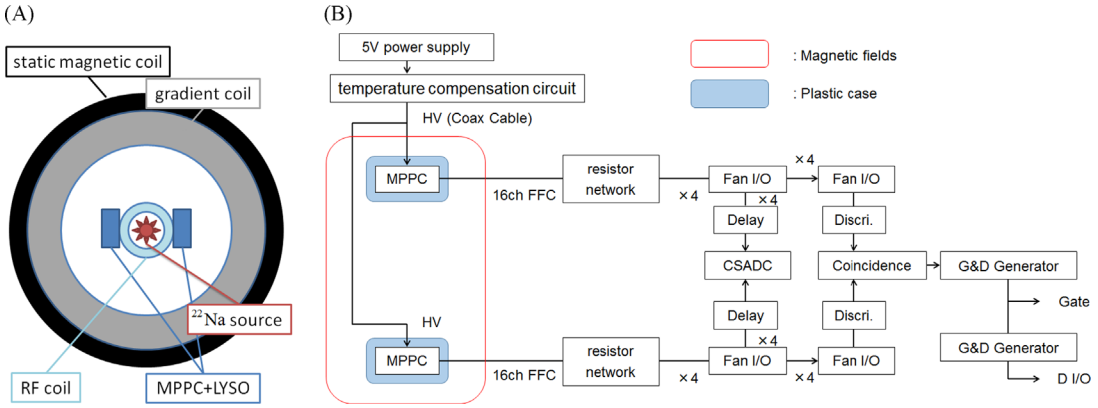

Fig. 2. Left: The experimental setup used for the imaging tests of PET. Right: The block diagram. We apply a voltage to the MPPC by passing through a 6-m coaxial cable. The signals from the MPPC pass through a 5-m flexible flat cable.

was fed into the charge-sensitive ADC (CSADC; HOSHIN V005), the other being summed over four signals to generate a trigger with a non-update discriminator (Technoland N-TM 405). Similarly, we processed the 16 signals from the other MPPC module, and two triggers (generated by discriminators) were fed into the coincidence module (Technoland N-TM 103). The gate width of the CSADC was set to 750 ns.

Fig. 4. The phantom used for MR imaging tests. This plastic cylinder filled with water.

In order to measure the influence from MRI, we took PET images outside the MRI, inside the MRI under fast spin echo operation (hereafter FSE), and under gradient echo operation (hereafter GE). Table 3 lists the parameters used for FSE multi-splice (FSEMS) and GE multi-slice (GEMS). The MRI system used for qualification tests is the Varian Unity-INOVA JASTEC Horizontal Magnet 4.7 T (JMTB-4.7/310/SS); the RF coil is the Varian Mouse Volume Quadrature Coil used for transmission and reception. These measurements were made for 20 min, respectively.

2.2. MR images operating with PET

In order to measure the influence from PET, we took MR images of the phantom in three ways: powering on the MPPC module

Table 4
Spatial resolution of a point ^{22}Na source image in FWHM.

	(A) outside	(B) under FSE	(C) under GE
x-Direction (mm)	1.63 ± 0.03	1.65 ± 0.07	1.70 ± 0.08
y-Direction (mm)	1.48 ± 0.03	1.49 ± 0.05	1.55 ± 0.13

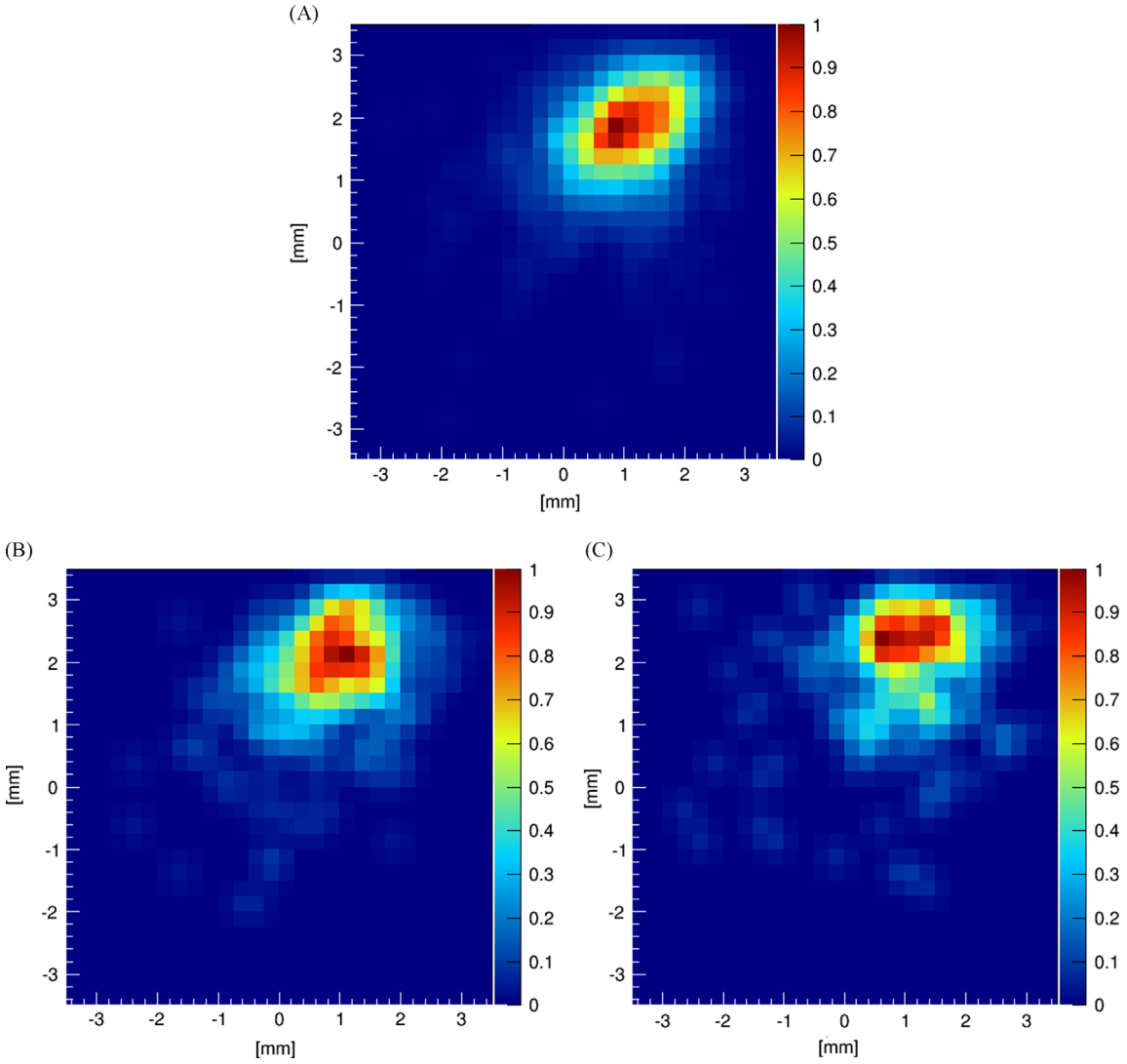

Fig. 5. The image of a point ^{22}Na source. (A) The MPPC module is outside MRI. (B) The MPPC module is inside MRI under FSE. (C) The MPPC module is inside MRI under GE. (A) outside MRI, (B) under FSE and (C) under GE.

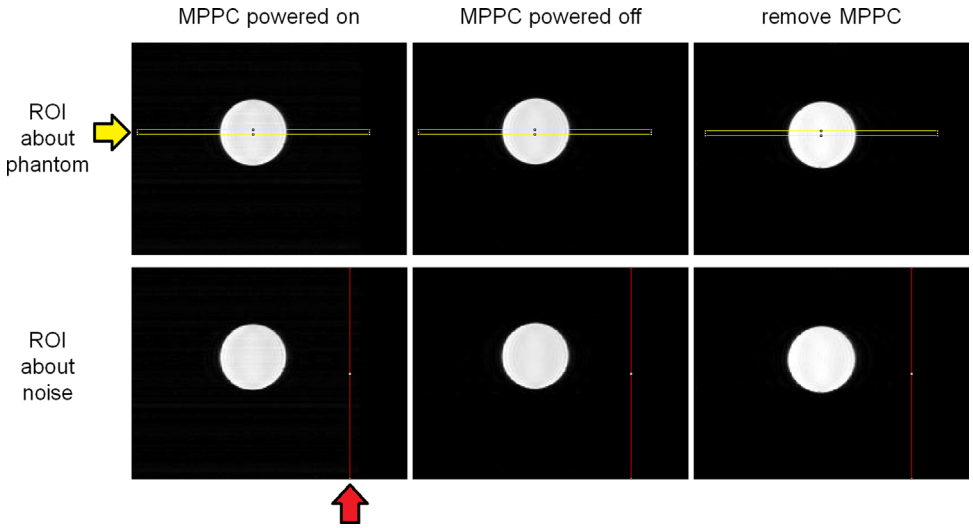

Fig. 6. The MR images (Cooperation of BioView Inc. (Japan)). These are the images when the MPPC module powered on is inside the MRI (left), when powered off inside the MRI (center), and when removed from the MRI (right). The top and bottom rows show the region of interaction between phantom and noise, respectively. (For interpretation of the references to color in this figure legend, the reader is referred to the web version of this paper.)

inside the MRI, powering off the MPPC module inside the MRI, and removing the MPPC module from the MRI. Fig. 4 shows the phantom used for this experiment. The scan time for these measurements is 5 min.

3. Results

3.1. Evaluations of PET images

Fig. 5 shows the PET images. These images suggest that the PET detector based on the MPPC can work well operating with MRI. In order to compare the spatial resolution with each other, we projected the source images onto profile histograms along the x-direction and the y-direction. Table 4 lists the x-direction or the y-direction spatial resolution for three images.

The x-direction resolutions when the MPPC module is inside MRI under FSE and GE were 1.65 ± 0.07 mm and 1.70 ± 0.08 mm (FWHM), respectively, while the x-direction resolution when the MPPC module is outside MRI was 1.63 ± 0.03 mm (FWHM). In the same way, the y-direction resolutions when the MPPC module is inside MRI under FSE and GE were 1.48 ± 0.03 mm and 1.49 ± 0.05 mm (FWHM), respectively, while the y-direction resolution when the MPPC module is outside MRI was 1.55 ± 0.13 mm (FWHM). While the degradation of image in terms of spatial resolution (FWHM) in the x- and y-directions is negligible, we see a slight distortion of the PET image operated under the MRI echo (Fig. 5).

3.2. Evaluations of MR images

Fig. 6 shows the MR slice images. The images are taken when the MPPC module powered on is inside the MRI (left), the MPPC module powered off is inside the MRI (center), and when the MPPC module is removed from the MRI (right). These images suggest that the MRI system can work well operating with PET. Fig. 7 (top) shows the profile histogram along the region enclosed by a yellow square of the slice images in the top row of Fig. 6. Red, green, and blue lines on the histogram represent the states where the MPPC powered on is inside MRI, the MPPC powered off is inside MRI, and the MPPC is removed from MRI, respectively.

We found degradation in the signal of MR images operating with PET. We evaluated the attenuation ratio, as expressed by the

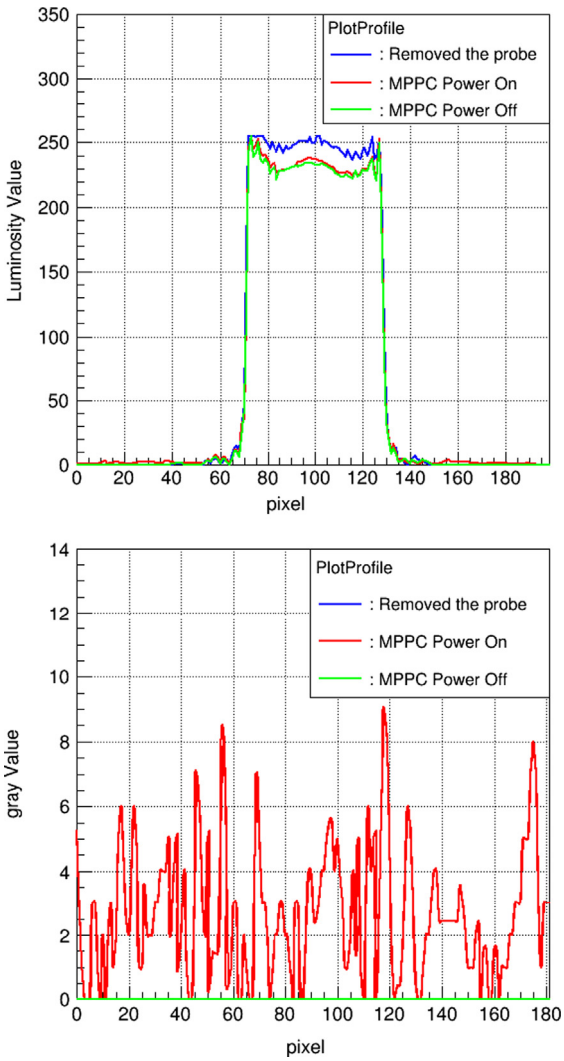

Fig. 7. Top: The profile histogram along the region enclosed by a yellow square of the slice images in the top row of Fig. 6. Bottom: The profile histogram along the red line region of the slice images in the bottom row of Fig. 6. (For interpretation of the references to color in this figure legend, the reader is referred to the web version of this paper.)

Fig. 8. The prototype gantry for MRI-PET. This gantry consists of eight MPPC-based PET modules, and is made of titanium and aluminum.

following equation:

$$\textit{Attenuation Ratio}\ [\%] = \frac{L_{on}(\textit{or}\ L_{off})}{L_{rm}} \times 100 \quad (1)$$

where L_{on}, L_{off}, and L_{rm} denote the luminosity values when the MPPC is powered on, powered off, and removed from MRI, respectively. The attenuation ratio for both ways was about 95%, suggesting that operating with PET has no great effect on MR images.

In order to examine the effect of noise, we also projected the red line of Fig. 6 onto the profile histograms shown in Fig. 7. This result suggests that the noise when the MPPC powered off is the same as when the MPPC is removed from MRI. In other words, there is no noise when the MPPC is powered off. Moreover, this result suggests that the noise when the MPPC powered on is only a few percent with respect to the signal value. Although improvements in the noise are needed, we can measure simultaneous PET and MR imaging without trouble.

4. Conclusion

This paper reported on the results of our high resolution, compact PET module for future MRI-PET. We only found slight degradation in the spatial resolution of PET images from 1.63 to 1.70 mm (FWHM; *x*-direction), or from 1.48 to 1.55 mm (FWHM; *y*-direction) when operating with the MRI. The signal-to-noise ratio (SNR) of the MRI image was only degraded by 5% operating with PET. Moreover, the noise of the MR image operating with PET was only a few percent with respect to the signal. Because PET and MRI have little impact on each other, we are now developing a more advanced version of the MRI-PET gantry with eight MPPC-based PET modules (Fig. 8).

References

[1] W.W. Moses, Nuclear Instruments and Methods in Physics Research Section A 471 (2001) 209.
[2] R.R. Raylman, et al., Nuclear Instruments and Methods in Physics Research Section A 569 (2006) 306.
[3] H. Peng, et al., Nuclear Instruments and Methods in Physics Research Section A 612 (2010) 412.
[4] S. Yamamoto, et al., Annals of Nuclear Medicine 24 (2010) 89.
[5] S. Yamamoto, et al., Physics in Medicine & Biology 55 (2010) 5817.
[6] C. Woody, et al., Nuclear Instruments and Methods in Physics Research Section A 571 (2007) 102.
[7] J. Kataoka, et al., IEEE Transactions on Nuclear Science NS-57 (5) (2010) 2448.
[8] T. Nakamori, et al., Journal of Instrumentation 7 (2012) C01083.
[9] H. Matsuda, et al., Nuclear Instruments and Methods in Physics Research Section A 699 (2013) 211.
[10] A. Kishimoto, et al., IEEE Transactions on Nuclear Science NS-60 (1) (2013) 38.
[11] J. Kataoka, et al., Nuclear Instruments and Methods in Physics Research Section A, 732 (2013) 403.
[12] T. Kato, et al., Nuclear Instruments and Methods in Physics Research Section A 638 (2011) 83.
[13] K. Sato, et al., IEEE Transactions on Nuclear Science Conference Record (NSS/MIC), 2010, p. 243.
[14] K. Yamamoto, et al., IEEE Transactions on Nuclear Science Conference Record, N24-292, 2007, p. 1511.
[15] I.G. Valais, et al., Nuclear Instruments and Methods in Physics Research Section A 569 (2006) 201.
[16] S. Siegel, et al., IEEE Transactions on Nuclear Science NS-43 (3) (1996) 1634.
[17] S. Vecchio, et al., Nuclear Instruments and Methods in Physics Research Section A 569 (2006) 264.
[18] T.Y. Song, et al., Physics in Medicine & Biology 55 (2010) 2573.
[19] T. Kato, et al., Nuclear Instruments and Methods in Physics Research Section A 699 (2013) 235.